RSC Advances

PAPER

View Article Online
View Journal | View Issue

Cite this: *RSC Adv.*, 2025, **15**, 13064

Investigating $Li_2Mg_2(WO_4)_3$: structure, morphology, and electrical properties with ultra-low dielectric loss for optimizing laser host materials

Mehdi Akermi,*[a] Ines Mbarek,[b] Rym Hassani,[c] Saber Nasri [b] and Abderrazek Oueslati *[b]

With technological advancements driving the demand for innovative materials, triple tungstate compounds, like $Li_2Mg_2(WO_4)_3$ (LMWO), offer exceptional properties for optoelectronic technologies. To investigate these potential outcomes, the LMWO compound was prepared *via* the solid-state reaction approach. The X-ray diffraction analysis revealed a single-phase material crystallizing in the orthorhombic structure, belonging to the *Pnma* space group. The crystallite size of the material was determined to be 58.32 nm, which played a significant role in enhancing its electrical performance. Scanning electron microscopy (SEM) revealed prismatic or rod-shaped particles with an average grain size of approximately 2.83 μm. Additionally, EDX confirmed the elemental composition, verifying the presence of Mg, W, and O, and ensuring the material's purity. Nyquist plots indicated non-Debye type relaxation, and further analysis of the relaxation frequency confirmed long-range motion of charge carriers. The temperature dependence of dielectric relaxation followed the Arrhenius law, yielding an activation energy of 0.84 eV. The frequency dependent behavior of M'' and Z'' at various temperatures indicated a shift from short-range to long-range mobility of charge carriers. The conductivity of the material increased with both temperature and frequency, demonstrating its semiconducting behavior. The temperature dependence of Jonscher's exponent suggests that conduction follows the non-overlapping small polaron tunneling (NSPT) model. This compound exhibited a high dielectric constant ($\varepsilon \sim 10^5$) and low dielectric loss at high frequencies, making it promising for applications in laser host materials and energy storage.

Received 19th December 2024
Accepted 4th April 2025

DOI: 10.1039/d4ra08888c

rsc.li/rsc-advances

Introduction

Tungstate oxides are highly promising materials thanks to their excellent ionic and electronic conductivity, as well as their ferroelectric, piezoelectric, and catalytic properties.[1–3] They are particularly appealing as solid-state laser host materials due to their high capacity for rare earth ion incorporation.[4–6] These compounds have a broad range of applications, including use as scintillation detectors and laser host materials, and in optical fibers.[7,8]

Transition metal oxides have recently gained significant attention as pseudo-capacitive materials because of their ability to exhibit multiple oxidation states, with examples including Ni,[9] Mo,[10] Co,[11] Mn,[12] W,[12] Cu,[12] and V.[12] However, single metal oxides still face issues such as toxicity, high cost, and low cycle life. In contrast, mixed metal oxides,[13] binary metal oxides,[14] and ternary metal oxides[15] often exhibit superior performance compared to their single-metal counterparts, owing to their varied oxidation states[16] and higher electrical conductivity.[17] Among the various double tungstates, the Li-based tungstates, $Li_xM_y(XO_4)_z$ where M = Al, In, Sc, Cr, Bi, Fe, Mg rare earth ion and X = Mo, W., are distinguished by their unique ionic conductivity and structural characteristics, making them pivotal materials for advancing energy storage and electrochemical devices.[18] The studies revealed that only four elements Cu, Fe, Mg, and Zn form double tungstates. Among these, the tetrahedral coordination of tungsten atoms was observed in $Li_2Mg_2(WO_4)_3$,[19] $Na_4Mg(WO_4)_3$,[20] $Na_4Zn(WO_4)_3$,[21] and $K_4Zn(WO_4)_3$,[22] while a wolframite-like structure was suggested for $Li_2Fe(WO_4)_2$ (ref. 23) and $Li_2Cu(WO_4)_2$.[24] Magnesium has been reported to form two double tungstates though with different stoichiometry $Li_2Mg_2(WO_4)_3$ (1 : 2 : 3)[25] and $Na_4Mg(WO_4)_3$ (2 : 1 : 3).[26] Following a comprehensive review of the literature, we have selected $Li_2Mg_2(WO_4)_3$ to synthesize in this study. The crystal structure of $Li_2Mg_2(WO_4)_3$ projected onto the

[a]*Nanotechnology research unit, Jazan University, P.O. Box. 114, Jazan 45142, Kingdom of Saudi Arabia. E-mail: makermi@jazanu.edu.sa*

[b]*Laboratory for Spectroscopic Characterization and Optics of Materials, Faculty of Sciences, University of Sfax, B.P. 1171, 3000 Sfax, Tunisia. E-mail: oueslatiabderrazek@yahoo.fr*

[c]*Environment and Nature Research Centre, Jazan University, P.O. Box. 114, Jazan 45142, Kingdom of Saudi Arabia*

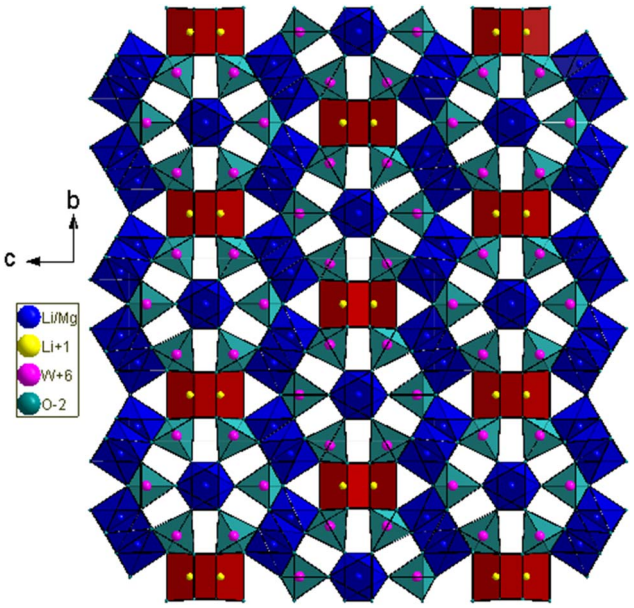

Fig. 1 Projection of crystal structure of $Li_2Mg_2(WO_4)_3$ into (100) plane.

(100) plane is depicted in Fig. 1. As shown, WO_4 units form tetrahedra with W atoms at their centers. The (1/3Li + 2/3Mg)O_6 units adopt an octahedral coordination, where (1/3Li + 2/3Mg) occupy the central position. Additionally, LiO_6 forms a prismatic structure with Li positioned at its center.[27]

This article aims to explore the morphological structure and electrical properties of a newly developed tungstate material. By examining its microstructural features and analyzing its conductivity, this study seeks to provide insights into how the material's composition and arrangement at the microscopic level influence its overall electrical behavior. Understanding these characteristics is essential for assessing the material's potential applications in advanced electronic devices and improving its performance for specific industrial purposes.

Experimental details

In this investigation, $Li_2Mg_2(WO_4)_3$ was prepared through a solid-state reaction technique. The starting materials consisted of ultra-pure WO_3, Li_2CO_3, and MgO. These materials were mixed in a molar ratio of $WO_3 : Li_2CO_3 : MgO = 3 : 1 : 2$ and pressed into a pellet. To compensate for lithium loss due to volatilization, an additional 2 mol% of Li_2CO_3 was added. The prepared mixture was first calcined at 750 °C for 35 h and was subjected to solid-state sintering at 900 °C for 120 hours in air, leading to the formation of the $Li_2Mg_2(WO_4)_3$ compound.

This extended sintering time was chosen to ensure complete phase formation, optimal crystallinity, and improved material properties. The prolonged sintering period allows the sample to undergo thorough structural refinement, reducing defects and promoting homogeneity. The furnace was maintained at a constant temperature throughout the 120-hour process, ensuring stable conditions for the sample during the entire sintering duration. Compounds in this family are commonly prepared at this temperature to achieve the desired material properties such as $Li_2Ni(WO_4)_2$, $Li_2Cu(WO_4)_2$, $Li_2Co(WO_4)_2$ which are prepared in 700 °C for 160 hours.[28] Also our compound under study is already studied with the same method.[27]

The crystal structure of the synthesized samples was examined using a Philips X'Pert X-ray powder diffractometer (XRD) with Cu Kα radiation ($\lambda = 1.5418$ Å). Data collection was conducted over a Bragg angle range of 10–60° at a scan rate of 0.05°/min. The structural refinement was performed through Rietveld analysis of the X-ray diffraction data, utilizing the FULLPROF software[29,30]

The microstructural features and elemental composition of the samples were examined using a FEI Nova NanoSEM 200 scanning electron microscope, integrated with an energy-dispersive X-ray spectroscopy (EDXS) analyzer.

Electrical measurements were conducted using two silver electrodes in an Ag/electrolyte/Ag configuration. The powder samples were pressed into tablets (8 mm in diameter and 1 mm in thickness) under a uniaxial pressure of 3 t cm^{-2}, with a silver conductive layer applied to both surfaces to serve as electrodes. Impedance measurements were performed across frequencies ranging from 0.1 Hz to 5 MHz using a 1260 Solartron Impedance Analyzer, controlled by a microcomputer, and carried out at temperatures between 473 and 673 K.

Results and discussion

Structural study

The X-ray diffraction (XRD) pattern of $Li_2Mg_2(WO_4)_3$, presented in Fig. 2, indicates that the sample is single-phase. All detected peaks correspond to an orthorhombic unit cell, belonging to the *Pnma* space group.

The crystal structure of $Li_2Mg_2(WO_4)_3$ was refined using the Rietveld method, with the refinement results summarized in Table 1 which are in good agreement with those determined from the published crystallographic data of $Li_2Mg_2(WO_4)_3$.[27] Considering the lattice parameters and the space group, the

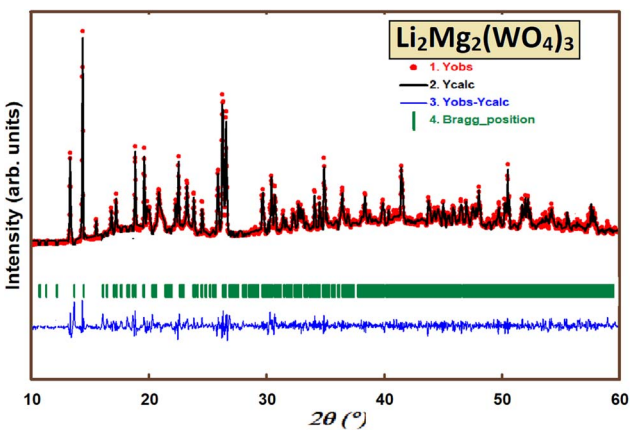

Fig. 2 The Rietveld refinement XRD of synthesized of LMWO at room temperature.

Table 1 Rietveld refined parameters and crystallite size for LMWO compound

$Li_2Mg_2(WO_4)_3$ compound at room temperature	
System	Orthorhombic
Space group	*Pnma*
Lattice parameters	
a	5.120 (±0.005)
b	10.502 (±0.006)
c	17.591 (±0.006)
α	90
β	90
γ	90
Reliability factors	
$R_p/R_{wp}/R_{exp}$	5.8%/7.9%/11.89%
χ^2	1.44
Crystallite size	58.32 nm

crystal structure of $Li_2Mg_2(WO_4)_3$ may be considered to be similar to that of $Li_2Fe_2(MoO_4)_3$ (ref. 31) and $Li_3Fe(MoO_4)_3$ (ref. 19) with W^{6+} tetrahedrally coordinated to four oxygen atoms.

As presented in Table 1, the reliability factors (R_{wp} and R_p) show excellent consistency between the experimental results and the theoretical calculations.

XRD analysis is utilized to calculate crystallite size. The average crystallite size (D) based on Debye–Scherrer equation can be calculated by[32,33]

$$D = \frac{K\lambda}{\beta_D \cos(\theta)} \quad (1)$$

Here, K represents the shape constant, which is equal to 0.9; λ denotes the wavelength of Cu Kα radiation; D is the full width at half maximum (FWHM) of the diffraction peak with the highest intensity among the other reflections; and θ is the diffraction angle. β denotes the full width at half maximum (FWHM) and quantifies the broadening of diffraction peaks, which is related to the crystallite size and internal strain in the material.

The D value is listed in Table 1. For double tungstate compounds, crystallite sizes in the nanometer range can lead to enhanced electrical properties, as well as improved conductivity and catalytic performance, often due to the increased surface area and quantum effects associated with nanostructured materials. As a result, we decided to conduct a comprehensive electrical study.

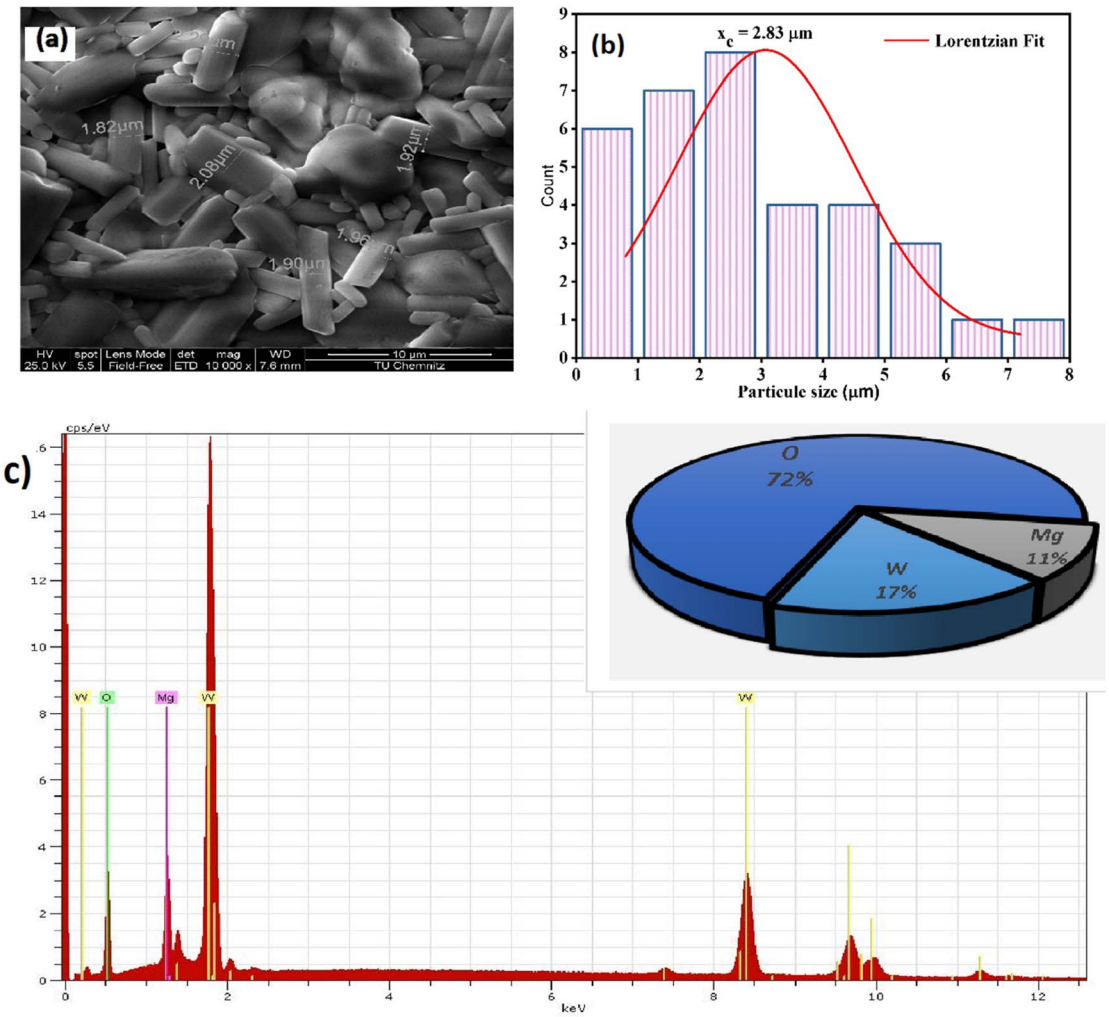

Fig. 3 (a) Scanning electron microscopy images, (b) distribution histogram of grains. (c) EDX spectrum of the compound LMWO.

Morphology analysis

Scanning electron microscopy (SEM) was employed to primarily examine the structural morphology of our material. In Fig. 3(a), SEM image presents the microstructure of the ceramic compound $Li_2Mg_2(WO_4)_3$, a lithium magnesium tungstate material. The morphology shows prismatic or rod-shaped particles in various sizes, with one measured at 4.90 μm in length, while others are smaller, measuring approximately 2.8 μm and 1.26 μm. These variations in size may indicate different growth orientations of the phase.

Fig. 3(b) depicts the grain count plotted against particle size (μm). The particle size distribution, obtained through ImageJ software, closely followed a Lorentzian fitting curve. Based on SEM analysis, the average grain size was determined to be 2.83 μm.

Energy dispersive X-ray microanalysis (EDX), as shown in Fig. 3(c), was employed to confirm the qualitative composition and assess the purity of the synthesized material. The identification of Mg, W, and O throughout the synthesis process confirmed that no elements were lost as the compound formed. Interestingly, lithium is not detected because its atomic number overlaps with that of the reference element used for this compound, beryllium. This study illustrates the uniformity of the synthesized $Li_2Mg_2(WO_4)_3$ sample.

Electrical properties

To gain insights into the electrical processes and conduction mechanisms within the $Li_2Mg_2(WO_4)_3$ compound, its electrical properties were investigated using complex impedance spectroscopy over a temperature range of 473–673 K. The Nyquist plot illustrates the relationship between the imaginary part of impedance (Z'') and the real part (Z'). Fig. 4 presents Nyquist plots for the $Li_2Mg_2(WO_4)_3$ ceramic at various temperatures. All spectra exhibit two semicircular arcs, with their centers positioned below the Z' axis. This indicates a relaxation behavior that deviates from the classical Debye model.[34]

The Nyquist plot of LMWO reveals two distinct arcs, which correspond to the responses of grain boundaries at lower temperatures and grains at higher temperatures, respectively.

The spectra were successfully modeled using a two-cell circuit model, consisting of two parallel combinations. The first component consists of a resistance (R_g) paired with a capacitance (C_g), whereas the second component includes a resistance (R_{gb}) in parallel with a constant phase element (CPE) and an additional capacitance (C_{gb}).[35]

The impedance of the fractal interface capacitance CPE is calculated as follows[36]

$$Z_{CPE} = \frac{1}{Q(j\omega)^{\alpha}} \quad (2)$$

Here, Q represents the capacitance value, and the parameter α describes the degree to which the semicircle of the component deviates from an ideal shape. Specifically, when $\alpha = 1$, the component behaves purely as a capacitor, while when $\alpha = 0$, it behaves as a resistor.

Based on the equivalent electrical circuit, the real part (Z') and the imaginary part (Z'') of the complex impedance can be expressed using the equations provided below:

$$Z' = \frac{R_g}{1 + (R_g C_g \omega)^2} + \frac{\frac{1}{R_g} + Q_0\omega^{\alpha}\cos\left(\frac{\alpha\pi}{2}\right)}{\left(\left(R^{-1} + Q_0\omega^{\alpha}\cos\left(\frac{\alpha\pi}{2}\right)\right)^2 + \left(C\omega + Q_0\omega^{\alpha}\sin\left(\frac{\alpha\pi}{2}\right)\right)^2\right)} \quad (3)$$

$$-Z'' = \frac{R_g C_g \omega}{1 + (R_g C_g \omega)^2} + \frac{C\omega + Q_0\omega^{\alpha}\sin\left(\frac{\alpha\pi}{2}\right)}{\left(\left(R^{-1} + Q_0\omega^{\alpha}\cos\left(\frac{\alpha\pi}{2}\right)\right)^2 + \left(C\omega + Q_0\omega^{\alpha}\sin\left(\frac{\alpha\pi}{2}\right)\right)^2\right)} \quad (4)$$

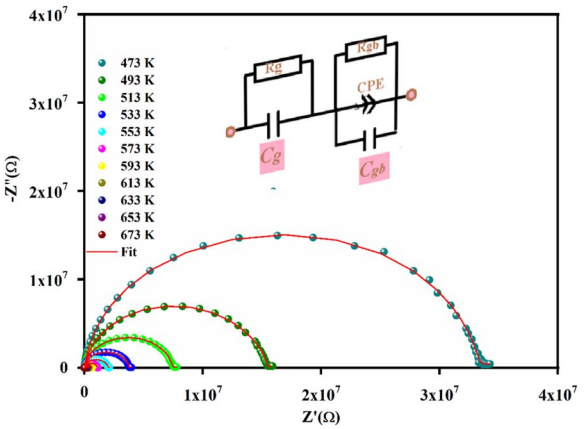

Fig. 4 Nyquist plot of LMWO compound, at different temperatures.

Fig. 5(a and b) illustrate the frequency-dependent relationship between the real part (Z') and the imaginary part (Z'') of the impedance within the temperature range of 473–673 K.

At each temperature point, the experimental (scatter) and theoretical (line) curves for both real and imaginary impedances closely align, indicating that the proposed circuit model accurately represents the behavior across the entire temperature range. Fig. 5(a) demonstrates that Z' decreases as both frequency and temperature increase, indicating that the material possesses negative temperature coefficient of resistance (NTCR) behavior.[37,38]

This behavior suggests that improving AC conductivity in $Li_2Mg_2(WO_4)_3$ could be achieved by increasing charge carrier mobility and decreasing trapped charge density. At high frequencies, Z' becomes less sensitive to temperature, indicating the presence of space charge within the material. As the frequency increases, the reduced relaxation time of the space charge leads to the convergence of the curves. This merging is attributed to a decrease in space charge polarization.[39]

In contrast, the fluctuations observed in the imaginary part Z'' (Fig. 5(b)) provide insights into the fundamental charge transport mechanism and the temperature-dependent

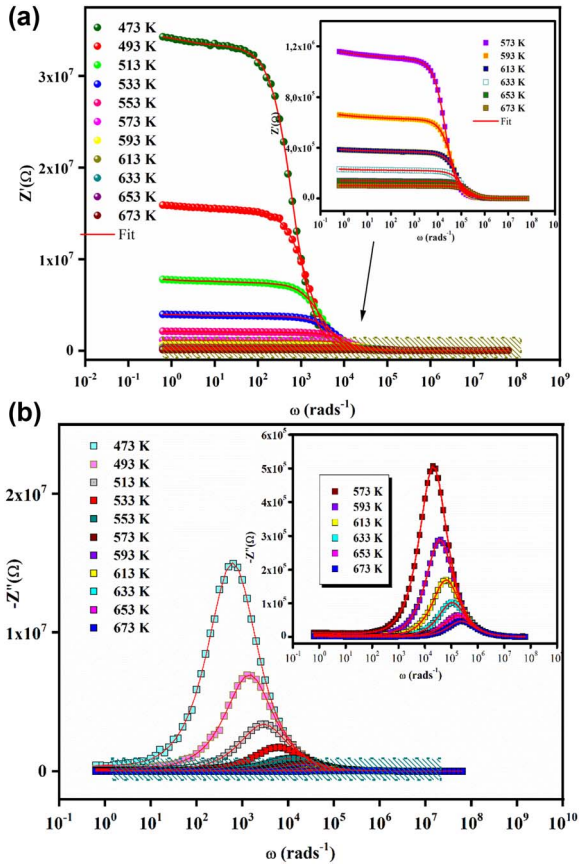

Fig. 5 (a): Frequency dependence of Z' at different temperatures. (b) Frequency dependence of Z'' at different temperatures.

relaxation process in $Li_2Mg_2(WO_4)_3$ .At lower temperatures, the relaxation process appears to be influenced by stationary species or electrons, while defects or vacancies play a more significant role at higher temperatures. Each spectrum shows a distinct peak known as the "relaxation frequency", which has a broad shape that deviates notably from ideal Debye behavior. At frequencies higher than the relaxation frequency, the movement of localized carriers is influenced by the extended transport of charge carriers, which primarily governs conduction processes below the loss peak frequency.

As the temperature increases, the relaxation peak shifts to higher frequencies, indicating a thermally activated relaxation process. Furthermore, the reduction in peak height with increasing temperature implies a decrease in the resistance of both the grains and grain boundaries.

The behavior of Z' and Z'' across the frequency range in our sample aligns with observations made in other ceramic systems reported in the existing literature.[40–42]

In Fig. 6, we present plots of $\frac{Z}{z''_{max}}$ and $\frac{d\frac{Z''}{z''_{max}}}{df}$ and for a temperature of 633 K to accurately determine the relaxation frequency Z''. The analysis reveals a shift in the relaxation frequency between the peak of the normalized impedance and the peak of its derivative. This shift confirms that the relaxation

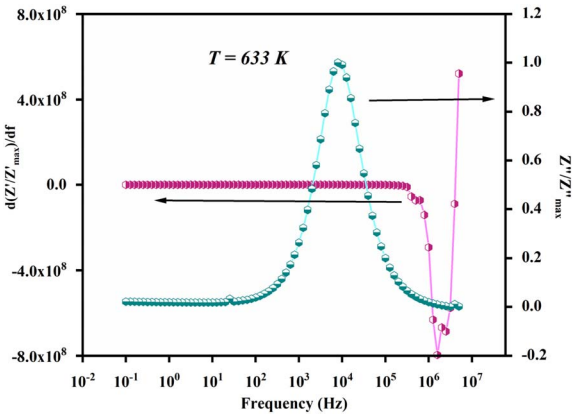

Fig. 6 Variation of Z''/Z''_{max} and M''/M''_{max} with frequency.

mechanism of our sample is non-Debye in nature.[43] Additionally, the relaxation model indicates that the behavior of the charge carriers is consistent with the temperature-dependent characteristics of the material.

Modulus analysis

A comprehensive analysis of the dielectric modulus offers a valuable method for investigating electrical transport phenomena in ceramics and for elucidating the microscopic mechanisms underlying dielectric relaxation[44]

The complex dielectric modulus, M^*, is expressed as the inverse of the complex dielectric constant.

$$M^* = \frac{1}{\varepsilon^*} = j\omega C_0 Z^* = M' + jM'' \quad (5)$$

where M' and M'' represent the real and imaginary parts of the dielectric modulus, respectively, while $C_0 = \frac{\varepsilon_0 A}{d}$ denotes the geometric capacitance (where ε_0 = vacuum permittivity, A = surface, d = thickness).

The complex modulus is expressed in terms of its real and imaginary components, as shown in the following expression

$$M' = \frac{\varepsilon'}{\varepsilon'^2 + \varepsilon''^2} \quad (6)$$

$$M'' = \frac{\varepsilon''}{\varepsilon' + \varepsilon''^2} \quad (7)$$

Here, ε' and ε'' denote the real and imaginary components of the dielectric permittivity, respectively.

Fig. 7 shows the variation of the real part of the modulus (M') with frequency at different temperatures. At lower frequencies, M' is nearly zero. As the frequency increases, M' steadily rises and eventually reaches a saturation point beyond a specific frequency. This characteristic frequency is temperature-dependent, and the amplitude of M' reaches a higher saturation level as the temperature rises. The phenomenon of saturation in M' is linked to charge transport behavior, which is governed by the mobility of available charge carriers. As temperature increases, the enhanced mobility of the charge

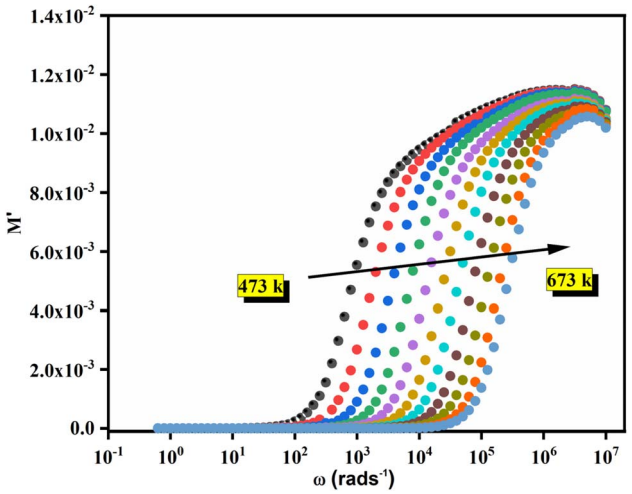

Fig. 7 Variation of M' with frequency at different temperatures for the entitled compound.

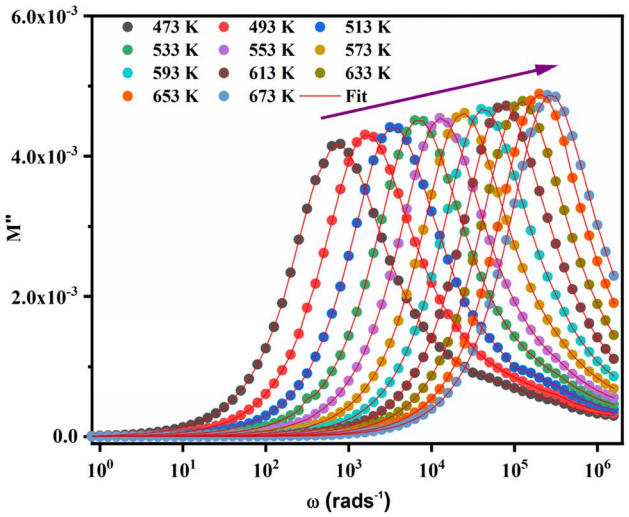

Fig. 9 Variation of M'' with frequency at different temperatures.

carriers leads to a higher overall saturation of M'.[45] Nevertheless, as the temperature rises, the movement of charge carriers is enhanced, leading to an increase in the overall saturation of M′ with temperature.[46]

At a fixed temperature, the maximum of M'' and minimum tangent points of M' coincide (Fig. 8), which agrees well with Bergman's fit.

In this context, the relaxation frequency corresponding to the M' peak signifies the transition between long-range and short-range dynamics as the frequency rises. The variation in temperature on the low-frequency side of the dielectric relaxation can be characterized using the Arrhenius equation. As a result, the activation energy (E_{relax}) is determined from:

$$\omega_{max} = \omega_0 \, e^{\left(-\frac{E_{relax}}{K_B T}\right)} \quad (8)$$

where ω_0 represents the preexponential term. Insert Fig. 8 shows the change in the relaxation time on a logarithmic scale

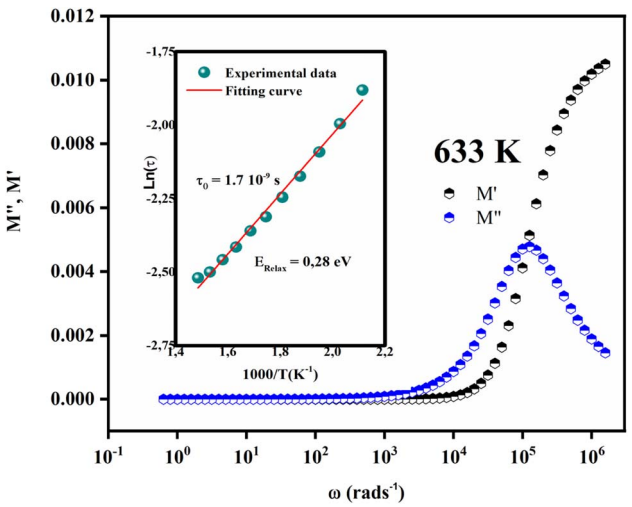

Fig. 8 Variation of M' and M'' as a function of ω at a fixed temperature (T = 633 K). (insert) The plot of ln(ω_{max}) *versus* 1000/T.

ln(τ) plotted against $10^3/T$ and ln (ω_{max}) as a function of 1000/T within the temperature range of 473–673 K. The key values for the relaxation energy and relaxation time, determined using the equation $\left(\tau_0 = \frac{1}{\omega_0}\right)$ are 0.82 eV and 1.7×10^{-9} s, respectively.

Fig. 9 illustrates the variation of the imaginary part of the modulus (M'') as a function of frequency, revealing three distinct regions. The first region occurs at low frequencies, below the peak maximum of M'' ($2\pi f^{M''}_{max}\tau_{M''} < 1$), where charge carriers exhibit long-range mobility, suggesting that ions can hop between adjacent sites. The second region corresponds to the high-frequency range, beyond the peak maximum of the M'' modulus ($2\pi f^{M''}_{max}\tau_{M''} > 1$), where the majority of charge carriers remain confined within their potential wells. In this region, charge carriers are restricted to short-range movement, demonstrating only localized motion within the potential well.[47] The final region corresponds to the peak of ($2\pi f^{M''}_{max}\tau_{M''} = 1$), where the transition from long-range to short-range mobility occurs. The imaginary part of M'' is fitted using the modified Kohlrausch–Williams–Watts (KWW) function, as proposed by Bergman.[48]

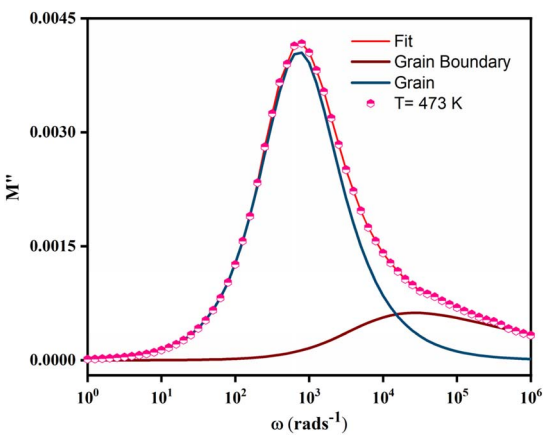

Fig. 10 Deconvolution of the modulus at T = 473 K.

$$M'' = \frac{M''_{max}}{(1-\beta)+\frac{\beta}{(1+\beta)}\left[\beta\left(\frac{\omega_{max}}{\omega}\right)+\left(\frac{\omega}{\omega_{max}}\right)^{\beta}\right]} \quad (9)$$

Here, M''_{max} represents the maximum value of M'', and ω_{max} denotes the corresponding maximum frequency.

The modulus deconvolution presented in Fig. 10 clearly reveals two contributions: one from the grain and the other from the grain boundary at the selected temperature of 473 K. We have chosen this temperature because at low temperatures, the deconvolution can be shown more clearly.

The complex modulus spectrum (M'' *vs.* M') for the $Li_2Mg_2(WO_4)_3$ compound displays semicircular arcs, as shown in Fig. 11. The spectrum clearly shows two prominent semicircles: the first at lower frequencies, attributed to grain effects, and the second at higher frequencies, corresponding to grain boundary effects. Additionally, a smaller semicircle appears at even higher frequencies, indicating the electrode effect. This behavior, depicted in the Nyquist plot in Fig. 4, supports the choice of the equivalent circuit model.

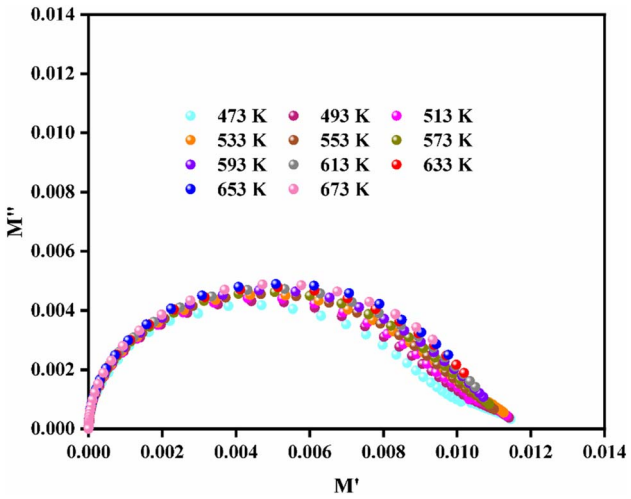

Fig. 11 Cole–Cole plots of modulus.

Fig. 12 illustrates the combined variation of M'' and Z'' with frequency at two different temperatures, 473 K and 673 K. Analyzing such curves is important because it provides information about the presence of the smallest capacitance and the largest resistance.[49] Additionally, the combined curve helps determine whether the relaxation process is associated with either short-range or long-range motion of charge carriers. If the peaks of Z'' and M'' are observed at different frequencies, the relaxation is linked to a short-range process. Conversely, for long-range motion, the peaks will coincide at the same frequency.[50] In the compound under investigation, the correspondence of the peaks at different temperatures suggests the presence of long-range motion of charge carriers and a deviation from non-Debye behavior[50] the variation of Z''/Z''_{max} and M''/M''_{max} with $\log\left(\frac{\omega}{\omega_{max}}\right)$ at both the lowest and highest temperatures for $Li_2Mg_2(WO_4)_3$ ceramics. The peaks of Z''/Z''_{max} and M''/M''_{max} do not coincide, confirming the non-Debye type relaxation behavior evident in the frequency-dependent results of the imaginary part of the modulus (Fig. 9). This same trend is observed at all other temperatures.[51]

AC conductivity

In Fig. 13 illustrates the variation of AC conductivity with frequency over a temperature range of 473 K to 673 K.

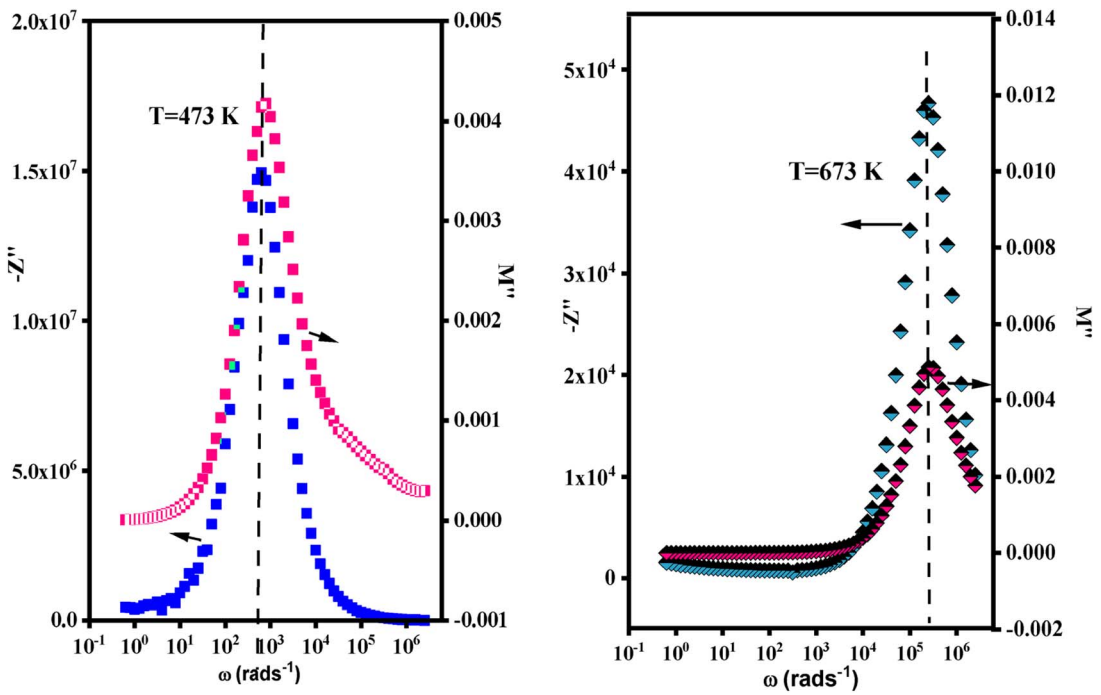

Fig. 12 $-Z''$& M'' variation with frequency at the highest and the lowest temperature.

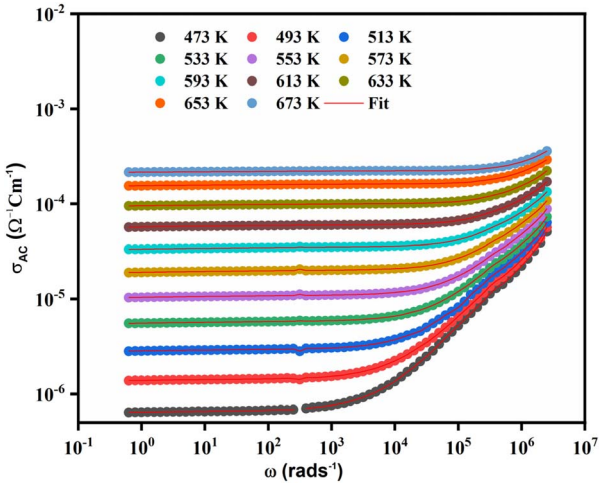

Fig. 13 Variation of σ_{AC} conductivity with temperature at different frequencies.

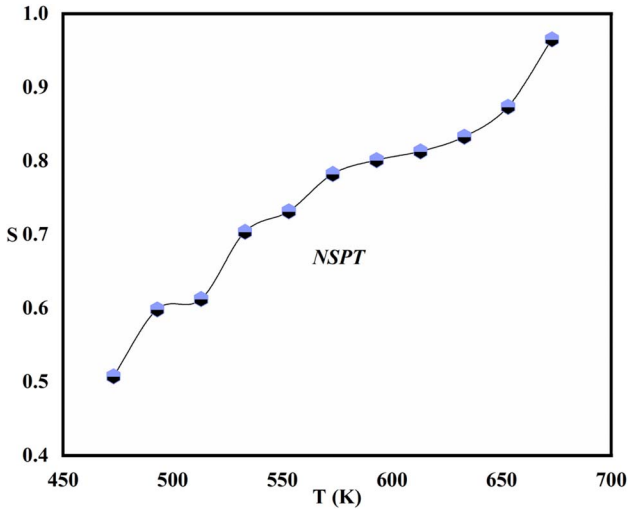

Fig. 14 Arrhenius fits of σ_{dc}.

The DC conductivity, observed at low frequencies, remains relatively stable and is not significantly influenced by frequency changes. In contrast, conductivity shows a frequency-dependent dispersion at high frequencies primarily attributed to AC conductivity. At low frequencies, charge carriers undergo activated hopping, leading to random diffusion and thus contributing to DC conductivity (σ_{dc}). During this frequency-dispersive region, ions move back and forth in a coordinated manner. Funke and Hoppe's jump relaxation model[12] explains the observed frequency-independent DC conductivity and the frequency-dependent AC conductivity. At lower frequencies, successful hops are the main contributors to conductivity, enabling long-distance ionic motion. The dispersion observed in the conductivity spectra is governed by the ratio of successful to failed hops. In the high-frequency range, an increase in failed hops results in greater dispersion.

The AC conductivity curve is modeled using the Jonscher power law:[52–55]

$$\sigma_{AC} = \sigma_{dc} + A\omega^{s} \quad (10)$$

Here, σ_{dc} represents the DC conductivity of the material; A is the pre-exponential factor, ω denotes the angular frequency, and s is the power-law exponent. The exponent s reflects the interaction between mobile ions and the adjacent lattice, with s generally varying between 0 and 1.[56] This range involves several physical processes such as quantum mechanical tunneling (QMT),[57] non-overlapping small polaron tunneling (NSPT),[58] correlated barrier hopping (CBH)[59] and overlapping large-polaron tunneling (OLPT).[60] Fig. 14 demonstrates that the exponent s increases with increasing temperature in the range from 473 to 673 K, suggesting that the NSPT model is suitable for describing the conduction mechanism in the material under study. σ_{dc} is obtained by fitting the Jonscher power law over the entire temperature range and is found to follow the Arrhenius relationship: Fig. 15 presents the dc electrical conductivity (σ_{dc}) plotted against the reciprocal of temperature, determined using parameters derived from complex impedance fitting.

This curve follows Arrhenius' law, which is expressed as:[61]

$$\sigma_{dc} = \sigma_0 \, e^{\left(\frac{-E_a}{K_B T}\right)} \quad (11)$$

This plot enables the determination of the activation energy, which is found to be 0.84 eV. The activation energy of the current substance seems to be within a range similar to that of the compounds previously studied,[62,63] which fall within the typical range of values characteristic of semiconductors.[64]

Insert Fig. 16 illustrates how the AC conductivity (σ_{ac}) changes with reciprocal temperature (1000/T) at constant frequencies for the compound under investigation. A linear segment is observed for each frequency. The data clearly show that the conductivity rises with both increasing frequency and temperature, which suggests that the sample exhibits semiconducting behavior. The higher value of the thermal activation

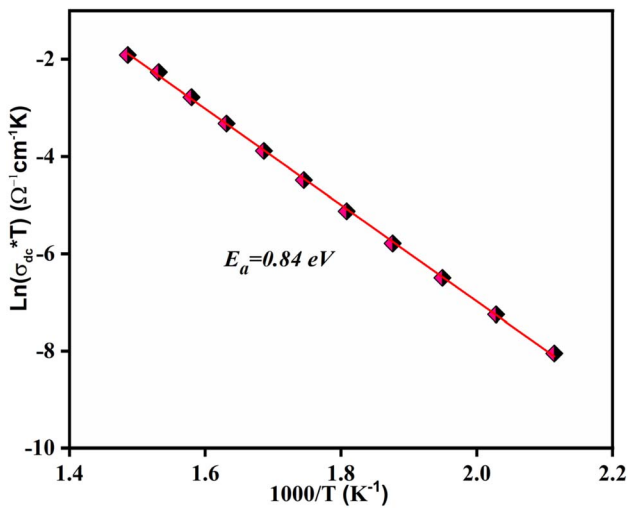

Fig. 15 Evolution of ln($\sigma_{dc}T$) as a function of (1000/T).

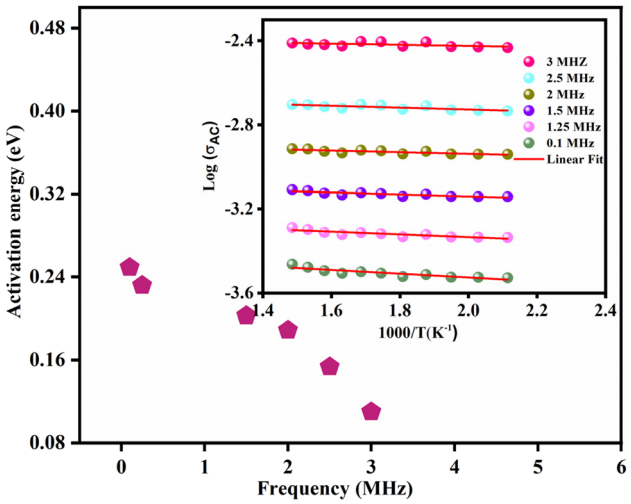

Fig. 16 Variation of the activation energy as a function of the frequency. (insert) Variation of the exponent *s* as a function of the temperature.

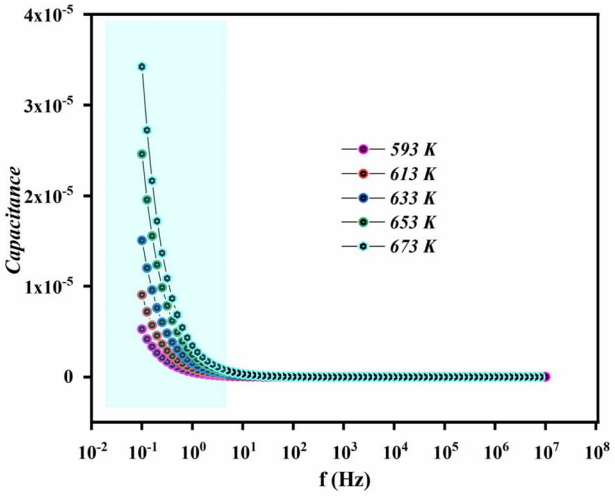

Fig. 17 Frequency dependence of capacitance spectra of LMWO.

energy for conduction, E_a, calculated from the slope of the curve, is observed in the low-frequency domain, whereas it is lower in the high-frequency domain (see Fig. 16). In the low-frequency region, the transport of charge carriers over longer distances requires less energy,[65] contributing to higher conductivity. In contrast, phenomena such as relaxation or orientation require more energy.[66] Additionally, the mobilities of vacancies (such as oxygen) along with cations at the grain boundaries can increase the activation energy at higher temperatures.

Dielectric

Fig. 17 depicts the change in capacitance as a function of angular frequency at various temperatures. The relationship between frequency and capacitance is clear, with capacitance decreasing as frequency increases. At lower frequencies, capacitance reaches its highest values, indicating the formation of inhomogeneous barriers at the interface due to interface states, which can generate an interfacial space charge. As seen in permittivity studies, capacitance initially decreases and then stabilizes. At 593 K, the capacitance values at lower frequencies are around 10^{-5} F. Consequently, higher capacitance could potentially enhance the performance of field-effect transistor (FET) devices.

Dielectric permittivity provides critical information about the properties of the material under study. It signifies the material's capacity to become polarized in response to an applied electric field. The dielectric behavior of a material is described by the complex dielectric constant:

$$\varepsilon^* = \varepsilon' - j\varepsilon'' = \frac{1}{j\omega C_0 Z^*} \quad (12)$$

ε' represents the real part of the dielectric permittivity, which indicates the energy stored, whereas ε'' represents the imaginary part, reflecting the energy loss within the material. C_0 is the capacitance of the vacuum, and ω is the angular frequency, defined as $\omega = 2\pi f$.

Additionally, the dielectric loss factor is defined as the quotient of the imaginary part (ε'') and the real part (ε') of the complex permittivity (ε^*).

$$\tan\delta = \frac{\varepsilon'}{\varepsilon''} \quad (13)$$

The study examines the variation of $\varepsilon'(\omega)$ and tan δ with frequency across the temperature range of 473–673 K. In Fig. 18, the frequency-dependent ε' values are shown at different temperatures. The sample exhibited higher ε' values at low frequencies, indicating their potential for low-frequency energy storage. As frequency increases, ε' values decrease, leading to a reduction in energy storage capacity. Additionally, at a given frequency, ε' values increase with temperature, indicating the thermal activation of charge carriers that affects polarization.

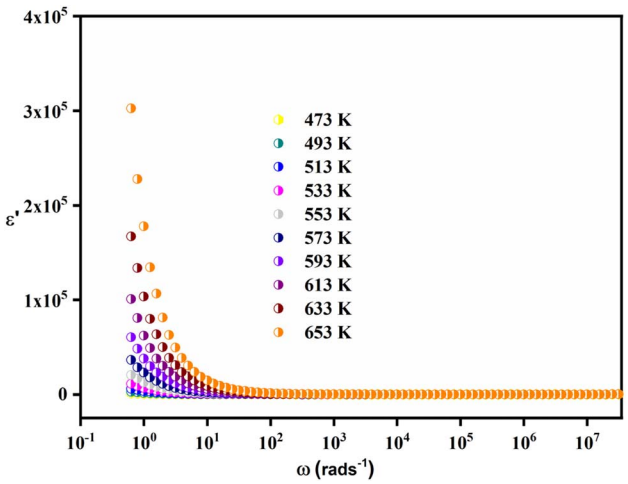

Fig. 18 Frequency-dependent real part (ε') of the dielectric permittivity.

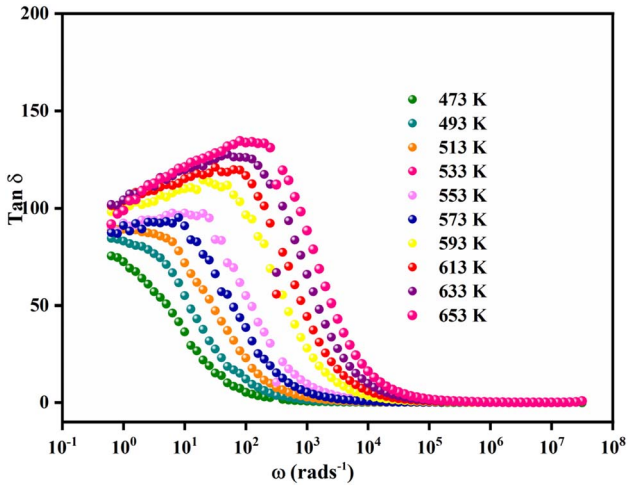

Fig. 19 tan(δ) *vs.* angular frequency spectra of LMWO.

This behavior is associated with four primary types of polarization: ionic, electronic, orientational, and interfacial. The polarizability of the system comprises relaxation components such as orientation and interfacial polarizations, along with resonance components that include ionic and electronic polarizations.

In contrast, for materials intended for optoelectronic applications, it is important to consider the "dissipation factor", represented as tan(δ) in Fig. 19. In this context, δ is the angle between the voltage and the charging current, often termed the "loss angle".[67] Dielectric loss results from several physical processes, including conduction, dielectric relaxation, molecular dipole moments, and interfacial polarization.[68] In the low-frequency range, more energy is needed to move charge carriers, resulting in higher tan(δ) values in this range. As the frequency increases, the material's resistivity decreases, allowing charge carriers to move more efficiently with less energy.[69] This characteristic leads to a reduction in dielectric loss at higher frequencies, underscoring the potential of these materials for electrical device applications. Furthermore, higher temperatures and lower frequencies contribute to increased dielectric loss, suggesting an improvement in the material's conductivity.[70]

Conclusion

With growing interest in double tungstate materials, we explore the structural, morphological, and electrical characteristics of the $Li_2Mg_2(WO_4)_3$ compound, synthesized using the solid-state reaction method. XRD analysis confirms the high crystallinity of the particles, identifying an orthorhombic structure with a *Pnma* space group. EDS elemental mapping demonstrates a homogeneous distribution of the constituent elements.

The influence of temperature on the relaxation and electronic transport processes in $Li_2Mg_2(WO_4)_3$ has been studied. In the study of AC conductivity, the universal power law model was utilized to examine the frequency-dependent behavior of the electrical data.

With its high dielectric constant ($\varepsilon \sim 10^5$) and low dielectric loss at high frequencies, this compound demonstrates strong potential for applications in laser host materials and energy storage.

Data availability

The authors confirm that the data used to support the findings of this study are included within the article and are available from the corresponding author upon reasonable request.

Conflicts of interest

The authors declare that they have no known competing financial interests or personal relationships that could have appeared to influence the work reported in this paper.

Acknowledgements

This article is derived from a research grant funded by the Research, Development, and Innovation Authority (RDIA) of the Kingdom of Saudi Arabia, with grant number 12894-JAZZAN-2023-JZU-R-2-1-SE.

References

1 X. Xu, *et al.*, Harvesting vibration energy to piezo-catalytically generate hydrogen through Bi2WO6 layered-perovskite, *Nano Energy*, 2020, **78**, 105351.
2 S. S. Hota, D. Panda and R. N. P. Choudhary, Structural, topological, dielectric, and electrical properties of a novel calcium bismuth tungstate ceramic for some device applications, *J. Mater. Sci.: Mater. Electron.*, 2023, **34**(10), 900.
3 F. Ahmad and S. Ahmad, 2D Metal Oxide Nanosheets—Electronic Applications Recent Developments and Future Prospects, *Advanced Applications of 2D Nanostructures: Emerging Research and Opportunities*, 2021, pp. 121–181.
4 Z. Chen, *et al.*, Emerging and perspectives in microlasers based on rare-earth ions activated micro-/nanomaterials, *Prog. Mater. Sci.*, 2021, **121**, 100814.
5 S. E. Crawford, P. R. Ohodnicki and J. P. Baltrus, Materials for the photoluminescent sensing of rare earth elements: challenges and opportunities, *J. Mater. Chem. C*, 2020, **8**(24), 7975–8006.
6 X. Xia, *et al.*, Quantum point defects for solid-state laser refrigeration, *Adv. Mater.*, 2021, **33**(23), 1905406.
7 C. Kim, *et al.*, A review of inorganic scintillation crystals for extreme environments, *Crystals*, 2021, **11**(6), 669.
8 B. Rekik, *et al.*, Optical properties of 2 at%(Ln3+) doped LiGd (WO4) 2 with Ln; Eu, Er and Tm, grown by μ-pulling down technique, *J. Alloys Compd.*, 2020, **830**, 154165.
9 X. Ge, *et al.*, Li2Ni (WO4) 2/C: a potential tungstate anode material for lithium ion batteries, *J. Alloys Compd.*, 2021, **888**, 161535.
10 N. Matskevich, *et al.*, Crystal growth and heat capacity of lithium molybdate tungstates, *Russ. J. Inorg. Chem.*, 2022, **67**(10), 1521–1526.

11 I. P. Muthuselvam, *et al.*, Two-step antiferromagnetic transition and moderate triangular frustration in Li 2 Co (WO 4) 2, *Phys. Rev. B: Condens. Matter Mater. Phys.*, 2014, **90**(17), 174430.
12 B. Wanklyn, F. Wondre and W. Davison, Flux growth of crystals of some magnetic oxide materials: Mn 7 SiO 12, CuO, MCr 2 O 4, MTiO 3, Ni 2 NbBO 6, MMoO 4 and Li 2 M 2 (MoO 4) 3,(M= Mn, Co, Ni), *J. Mater. Sci.*, 1976, **11**, 1607–1614.
13 X. Liu, *et al.*, Noble metal–metal oxide nanohybrids with tailored nanostructures for efficient solar energy conversion, photocatalysis and environmental remediation, *Energy Environ. Sci.*, 2017, **10**(2), 402–434.
14 Y. Zhang, *et al.*, Binary metal oxide: advanced energy storage materials in supercapacitors, *J. Mater. Chem. A*, 2015, **3**(1), 43–59.
15 A. Walsh, *et al.*, Oxidation states and ionicity, *Nat. Mater.*, 2018, **17**(11), 958–964.
16 M. B. Schütz, *et al.*, Microwave-assisted synthesis of nanocrystalline binary and ternary metal oxides, *Int. Mater. Rev.*, 2018, **63**(6), 341–374.
17 F. Hong, *et al.*, Significant improvement in Mn2O3 transition metal oxide electrical conductivity *via* high pressure, *Sci. Rep.*, 2017, **7**(1), 44078.
18 K. S. Dhindsa, *Enhancement in Electrochemical Performance of LiFePO4-Carbon Nano Composite Materials for Lithium Ion Batteries*, Wayne State University, 2015.
19 S. Chen, *et al.*, Lithiated bimetallic oxide, Li3Fe (MoO4) 3, as a high-performance anode material for lithium-ion batteries and its multielectron reaction mechanism, *J. Power Sources*, 2020, **476**, 228656.
20 Y. Xiao, D. Yan and D. Wu, Comment on "Bandshift luminescence thermometry using Mn4+: Na4Mg (WO4) 3 phosphors", *Chem. Mater.*, 2020, **32**(22), 9813–9816.
21 A. Buzlukov, *et al.*, Revealing sodium-ion diffusion in alluaudite-type Na4–2xM1+ x (MoO4) 3 (M= Mg, Zn, Cd) from 23Na MAS NMR and *ab initio* studies, *J. Solid State Chem.*, 2021, **293**, 121800.
22 R. Klevtsova, N. Ivannikova and P. Klevtsov, Crystal structure and polymorphism of potassium zinc tungstate K 4 Zn (WO 4) 3, *Kristallografiya*, 1979, **24**(2), 257–264.
23 P. Klevtsov, N. Novgorodtseva and L. Y. Kharchenko, Hydrothermal Synthesis of the Tungstates Li 2 Fe (WO 4) 2 and Li 2 WO 4 and Their Thermographic and X-Ray Investigation, in *Soviet Physics Doklady*, 1969.
24 A. Mahieddine, *et al.*, Synthesis, characterization, and effect of electrolyte concentration on the electrochemical performance of Li2Cu (WO4) 2 as a high-performance positive electrode for hybrid supercapacitors, *J. Energy Storage*, 2022, **56**, 106011.
25 H. Zhu, *et al.*, Photoluminescence properties of Li2Mg2 (WO4) 3: Eu3+ red phosphor with high color purity for white LEDs applications, *J. Lumin.*, 2016, **172**, 180–184.
26 D. K. Amarasinghe and F. A. Rabuffetti, Bandshift luminescence thermometry using Mn4+: Na4Mg (WO4) 3 phosphors, *Chem. Mater.*, 2019, **31**(24), 10197–10204.
27 Z. Fu and W. Li, Crystal structure of a new compound Li2Mg2 (WO4) 3, *Powder Diffr.*, 1994, **9**(3), 158–160.
28 K. Karoui, *et al.*, Electrical and electrochemical properties of Li 2 M (WO 4) 2 (M= Ni, Co and Cu) compounds, *RSC Adv.*, 2019, **9**(12), 6785–6792.
29 H. M. Rietveld, A profile refinement method for nuclear and magnetic structures, *J. Appl. Crystallogr.*, 1969, **2**(2), 65–71.
30 R. Bandyopadhyay, *et al.*, Application of powder X-ray diffraction in studying the compaction behavior of bulk pharmaceutical powders, *J. Pharmaceut. Sci.*, 2005, **94**(11), 2520–2530.
31 C. Torardi and E. Prince, Structure of the lithium insertion compound Li2Fe2 (MoO4) 3 from neutron powder diffraction data, *Mater. Res. Bull.*, 1986, **21**(6), 719–726.
32 S. Yousefi, B. Ghasemi and M. P. Nikolova, Morpho/Opto-structural characterizations and XRD-assisted estimation of crystallite size and strain in MgO nanoparticles by applying Williamson–Hall and size–strain techniques, *J. Cluster Sci.*, 2022, **33**(5), 2197–2207.
33 N. Rani, *et al.*, Role of oxygen vacancies for mediating ferromagnetic ordering in La-doped MgO nanoparticles, *J. Supercond. Novel Magn.*, 2020, **33**, 1473–1480.
34 S. Chaouachi, B. Hamdi and R. Zouari, Crystal structure, electrical study and dielectric behavior of a new centrosymmetric hybrid material, *Synth. Met.*, 2017, **223**, 122–131.
35 P. Aswathy, R. Ganga and D. N. Rajendran, Impact of A-site calcium on structural and electrical properties of samarium cobaltite perovskites, *Solid State Commun.*, 2022, **350**, 114748.
36 P. Córdoba-Torres, T. J. Mesquita and R. P. Nogueira, Relationship between the origin of constant-phase element behavior in electrochemical impedance spectroscopy and electrode surface structure, *J. Phys. Chem. C*, 2015, **119**(8), 4136–4147.
37 D. Panda, S. S. Hota and R. Choudhary, Synthesis of a scheelite barium molybdate: Structural, topological, electrical, and transport properties for negative temperature coefficient thermistor application, *J. Solid State Chem.*, 2024, **331**, 124531.
38 B. K. Das, T. Das and D. Das, Structural and electrical properties of mechanically alloyed ZnO nanoceramic for NTC thermistor application, *J. Mater. Sci.: Mater. Electron.*, 2023, **34**(3), 230.
39 G. Fang, *et al.*, Determining the preferable polarization loss for magnetoelectric microwave absorbers by strategy of controllably regulating defects, *Chem. Eng. J.*, 2023, **463**, 142440.
40 X. Lin, H. Gong and Z. Chen, Fabrication of SiCN (Fe)/Al2O3 wave-absorbing ceramics with enhanced electromagnetic performance, *Ceram. Int.*, 2023, **49**(14), 23851–23863.
41 J. Su, *et al.*, Thin La doped CaMnO3 ceramics for attenuation– impedance balance to facilitate excellent microwave absorption, *Ceram. Int.*, 2023, **49**(19), 32049–32057.

42 Z. Lu, *et al.*, Energy storage properties in Nd-doped AgNbTaO3 lead-free antiferroelectric ceramics with Nb-site vacancies, *J. Adv. Dielectr.*, 2023, **13**(01), 2242006.
43 M. Javed, *et al.*, Charge conduction mechanism and non-debye type relaxation in LaCrO3 perovskite orthochromite, *Mater. Chem. Phys.*, 2022, **290**, 126522.
44 S. Patil, *et al.*, Molecular mechanism of the Debye relaxation in monohydroxy alcohols revealed from rheo-dielectric spectroscopy, *Phys. Rev. Lett.*, 2023, **130**(9), 098201.
45 S. Anirban, R. Roy and A. Dutta, Microstructure, charge carrier conduction mechanism model, dielectric properties and leakage current analysis of Dy2FeMnO6 nanomaterial, *Ceram. Int.*, 2023, **49**(8), 12334–12347.
46 A. S. Jbara, *et al.*, Density functional theory study of mixed halide influence on structures and optoelectronic attributes of CsPb (I/Br) 3, *Appl. Opt.*, 2020, **59**(12), 3751–3759.
47 S. K. Barik, R. Choudhary and A. Singh, Ac impedance spectroscopy and conductivity studies of Ba0. 8Sr0. 2TiO3 ceramics, *Adv. Mater. Lett.*, 2011, **2**(6), 419–424.
48 R. Bergman, General susceptibility functions for relaxations in disordered systems, *J. Appl. Phys.*, 2000, **88**(3), 1356–1365.
49 D. C. Sinclair and A. R. West, Impedance and modulus spectroscopy of semiconducting BaTiO3 showing positive temperature coefficient of resistance, *J. Appl. Phys.*, 1989, **66**(8), 3850–3856.
50 N. Panda, *et al.*, Structural, dielectric and electrical properties of the Ba 2 BiNbO 6 double perovskite, *J. Mater. Sci.: Mater. Electron.*, 2015, **26**, 3797–3804.
51 S. Brahma, R. Choudhary and A. K. Thakur, AC impedance analysis of LaLiMo2O8 electroceramics, *Phys. B*, 2005, **355**(1–4), 188–201.
52 K. Funke and R. Hoppe, Jump-relaxation model yields Kohlrausch-Williams-Watts behaviour, *Solid State Ionics*, 1990, **40**, 200–204.
53 I. Garoui, *et al.*, Lead-Free Halide Perovskites for optoelectronic application: Investigation of Structural, Optical, Electric and Dielectric behaviors, *Opt. Mater.*, 2024, 115664.
54 K. Krishna, *et al.*, Mg2+-induced luminescence enrichment and dielectric investigations on Ca (WO4): Tm3+/Yb3+, *Opt. Mater.*, 2024, **154**, 115623.
55 A. Al-Muntaser, *et al.*, Tuning the structural, optical, electrical, and dielectric properties of PVA/PVP/CMC ternary polymer blend using ZnO nanoparticles for nanodielectric and optoelectronic devices, *Opt. Mater.*, 2023, **140**, 113901.
56 I. Kammoun, *et al.*, Investigation of structural, optical and electrical conductivity of a new organic inorganic bromide:[C 12 H 17 N 2] 2 ZnBr 4, *RSC Adv.*, 2023, **13**(12), 8034–8042.
57 M. Rani, R. C. Pawar and N. Panwar, Exploring the comparison of optical, dielectric and photocatalytic performance of Yb3+ and Gd3+ half-doped DyCrO3 nanostructures, *Mater. Chem. Phys.*, 2024, **314**, 128848.
58 M. Krichen, *et al.*, Structural, optical and electrical properties of NiMO4 (M= W and Mo), *J. Mol. Struct.*, 2024, **1298**, 137116.
59 M. L. Bouazizi, *et al.*, Sol-gel synthesis and property studies of Cu0. 4Mg0. 4Co0. 2FeCrO4 spinel ferrite for optoelectronic, magnetic, and electrical applications, *Opt. Mater.*, 2024, **149**, 115059.
60 M. Abdel-baki, S. Ibrahim and G. M. Turky, Role of SnO2 on the structural, optical, thermal conductivity, and electrical characteristics of multicomponent borate glasses, *Opt. Mater.*, 2024, **149**, 115048.
61 J. Zhang, *et al.*, Impact of non-bridging oxygens on the thermal, electrical and optical properties of germanate glasses and exploration of the germanate anomaly, *Ceram. Int.*, 2024, **50**(9), 14020–14030.
62 N. Yadav and A. Khare, Minimization of carrier recombination in La2NiMnO6 double perovskite solar cells by optimizing defects and band offsets, *Phys. Scr.*, 2023, **98**(7), 075917.
63 D. S. GT and R. Bhowmik, Doping of large amount tetravalent Ge ions into Fe2O3 structure and experimental results on modified structural, optical and electronic properties, *Mater. Sci. Semicond. Process.*, 2024, **170**, 107949.
64 M. Naher, *et al.*, A comprehensive *ab-initio* insights into the pressure dependent mechanical, phonon, bonding, electronic, optical, and thermal properties of CsV3Sb5 Kagome compound, *Results Phys.*, 2023, **51**, 106742.
65 A. Páez, *et al.*, Comparing distance, time, and metabolic energy cost functions for walking accessibility in infrastructure-poor regions, *J. Transport Geogr.*, 2020, **82**, 102564.
66 C. E. Jackson, *et al.*, A reaction-coordinate perspective of magnetic relaxation, *Chem. Soc. Rev.*, 2021, **50**(12), 6684–6699.
67 D. Nayak, *et al.*, Effect of Nanofillers-Reinforced Polymer Blends for Dielectric Applications, in *Emerging Nanodielectric Materials for Energy Storage: from Bench to Field*, Springer, 2023, pp. 151–187.
68 L. Zhu, Exploring strategies for high dielectric constant and low loss polymer dielectrics, *J. Phys. Chem. Lett.*, 2014, **5**(21), 3677–3687.
69 H. F. Haneef, A. M. Zeidell and O. D. Jurchescu, Charge carrier traps in organic semiconductors: a review on the underlying physics and impact on electronic devices, *J. Mater. Chem. C*, 2020, **8**(3), 759–787.
70 R. Li, *et al.*, Review on polymer composites with high thermal conductivity and low dielectric properties for electronic packaging, *Mater. Today Phys.*, 2022, **22**, 100594.